Improvement of remeshed Lagrangian methods for the simulation of dissolution processes at pore-scale

Jean-Matthieu Etancelin[a], Peter Moonen[b,c], Philippe Poncet[a]

[a] *Universite de Pau et des Pays de l'Adour, E2S UPPA, CNRS, LMAP, Pau, France.*
[b] *Universite de Pau et des Pays de l'Adour, E2S UPPA, CNRS, Total, LFCR, Pau, France.*
[c] *Universite de Pau et des Pays de l'Adour, E2S UPPA, CNRS, DMEX, Pau, France.*

Abstract

This article shows how to consistently and accurately manage the Lagrangian formulation of chemical reaction equations coupled with the superficial velocity formalism introduced in the late 80s by Quintard and Whitaker. Lagrangian methods prove very helpful in problems in which transport effects are strong or dominant, but they need to be periodically put back in a regular lattice, a process called remeshing. In the context of digital rock physics, we need to ensure positive concentrations and regularity to accurately handle stagnation point neighborhoods. These two conditions lead to the use of kernels resulting in extra-diffusion, which can be prohibitively high when the diffusion coefficient is small. This is the case especially for reactive porous media, and the phenomenon is reinforced in porous rock matrices due to Archie's law. This article shows how to overcome this difficulty in the context of a two-scale porosity model applied in the Darcy-Brinkman-Stokes equations, and how to obtain simultaneous sign preservation, regularity and accurate diffusion, and apply it to dissolution processes at the pore scale of actual rocks.

Keywords: Three-dimensional flows, Digital Rock Physics, Reactive flows, Dissolution process, Lagrangian methods, Porous media.

1. Introduction

Dissolution processes at pore scale play a crucial role in a wide range of applications. For example, mineral dissolution alters the hydraulic conductivity of soils [57] and calcite dissolution in seawater is a key mechanism affecting the global carbon budget of the planet [41]. Several emerging technologies rely on an in-depth understanding of dissolution mechanisms, such as the storage of natural gas in underground caverns located in deep salt domes [9], the assessment of the long-term storage capacity of CO_2 in carbonate formations [22, 50], and the chemical stimulation of geothermal reservoirs [35]. Other industrial processes, such as water desalination, also rely on the dissolution of $CaCO_3$ [31].

The modeling of reactive transport and dissolution at pore scale is currently still a challenge. In the context of CO_2 sequestration, Liu et al. (2019) highlighted the need to develop numerical schemes meeting requirements of stability and convergence, as well as local mass conservation and minimal numerical diffusion [34]. Steefel et al. (2005) advocated for the use of reactive transport models in earth sciences, yet stressed that capturing the scale-dependence of reactive transport processes is a challenge yet to be overcome [54]. As a concrete example of this scale-dependence, we can cite the work of Gray et al. [21]. Confronting experimental results with simulations of calcite dissolution in HCl showed that small morphological features, such as pore-throat size, micro-porosity and specific reactive area, could have a significant impact on the reaction rates and the dissolution patterns obtained. Li et al. (2006) focused their attention on another scale-related challenge, namely sign-preservation [32]. More precisely, the use of volume-averaged concentrations might lead locally to an erroneous prediction of the reaction direction, *i.e.* dissolution instead of crystallization or vice versa. The preceding overview aims to clarify that, while the governing partial differential equations for reactive transport modeling are largely understood, they remain difficult to implement.

Many models and related numerical methods have been developed in order to investigate pore-scale physics and mechanics. These reactive hydrodynamic models are mainly based on surface reactions or volume reactions. Surface reactions are well-suited to mesh-based methods (Finite Volumes [39, 43], Finite Elements [2, 6], Lattice Boltzmann Methods [25], ALE [52], Boundary Element Methods [33, 8, 45], etc.), while volume reactions allow most of the usual numerical methods (including LBM [58, 27], FV [51] and SPH [7]) but require clever modeling of surface-localized phenomena. Volume based modeling using structured meshes can involve crude no-slip conditions fusing penalization techniques [3, 16], but nowadays two-scale models are suitably formalized [42, 38, 51], allowing greater physical involvement of the rock matrix in the samples.

In this work, we are proposing a method to tackle some of these issues. We suggest coupling a Lagrangian formulation of the chemical equations with the superficial velocity formalism introduced in the late 80s by Quintard

and Whitaker [46, 47]. The velocity formulation relies on a two-scale scalar porosity field representing the micro-porosity of the rock, which can degenerate to 100% to model pure fluid regions (macro-porosity). The appropriate fluid transport equations are recovered in both regions. Ion transport is governed by a particle method that has been modified in order to accurately handle both diffusion and convection-dominated regions. Care has been taken to ensure that the chemical reaction consistently modifies the micro- and macro-porosity, and thus the specific reactive area.

Lagrangian and particle methods are especially well-suited to transport-dominant phenomena, but most of the time, an accurate remeshing step must be periodically performed in order to avoid disorganized particle distributions [15, 28]. Convolving with second-order and higher kernels does not preserve the sign. However, digital rock physics modeling requires ensuring the sign preservation of quantities (in chemical terms). Consequently, from a mathematical point of view this is possible only if a relatively inaccurate diffusive remeshing process is used. Moreover, in this study we couple several physical phenomena thereby requiring state-variables on both particles and grids, hence the need for detailed remeshing and interpolation. Using smooth and/or high order interpolation kernels provides a good contrast on state variables and avoids the concentration of particles on interfaces and fronts.

The present article describe a technique to overcome these two difficulties: how to estimate the diffusion induced by remeshing and thereby adapt the physical diffusion, and how and when to switch from a low-order to a high-order convolution, the aim being to minimize the remeshing diffusion when the physical diffusion is too small to be adapted.The objective is to introduce a 3D numerical method and apply it in order to perform long-time dissolution of real geometries in 3D. Nevertheless, validation is achieved by means of a benchmark problem in 2D, and 1D examples are given to illustrate numerical analyze.

Section 2 describes the governing equations of reactive transport (one liquid phase) through a heterogeneous porous medium, including a porous rock matrix and fluid pore space. Section 3 explains the Lagrangian formulation of reactive transport, the remeshing procedure, and illustrates the weaknesses of several straightforward strategies, more particularly over-diffusion and instability. The *a posteriori* kernel selection technique is then presented to answer the question, and includes a numerical illustration of a variable diffusion heat equation. Section 4 is dedicated to the numerical implementation of the model, based on a hybrid GPU-CPU implementation of the method. In section 5, we put into practice the full reaction-transport-diffusion equation with superficial velocity feedback in porous media. First, for the validation step, in section 5.1, we consider the dissolution of a 2D calcite core, following the configuration of the benchmark described in [38]. Second, in section 5.2, we consider the dissolution process in a high-resolution 3D image of a real carbonate rock obtained by microCT [19]. This makes it possible to follow the wormhole formation in a heterogeneous media, here a non-percolating medium whose pore space is composed of fluid inclusions. Third, in order to exhibit a wormholing regime in a more conventional porous medium, we consider in the section 5.3 a percolating sandstone (featuring a porosity of 28% and a permeability around $10^{-11}\mathrm{m}^2$), whose evolution is computed until 70% of its mass is dissolved.

2. Governing equation of reactive transport

2.1. Superficial velocity

The superficial velocity u of a viscous fluid in a porous medium can be modeled by the Darcy-Brinkman-Stokes (DBS) equation [47] :

$$\begin{aligned}\varepsilon^{-1}\frac{\partial(\rho u)}{\partial t} + \varepsilon^{-1}\mathrm{div}\left(\varepsilon^{-1}\rho u\otimes u\right)\\ -\varepsilon^{-1}\mathrm{div}\,(\mu D(u)) + \mu^* K^{-1}u = f - \nabla p,\end{aligned} \tag{1}$$

where porosity is denoted ε and permeability K, pressure p, density ρ, shear-rate $D(u) = (\nabla u + \nabla u^T)/2$, dynamic viscosity μ and external force f. The deviated viscosity μ^*, often chosen as being equal to μ, can take into account the deviation of thermodynamic or chemical properties due to the strong variations in porosity. This equation goes together with the incompressibility condition $\mathrm{div}\,u = 0$ when density remains constant, but can be non-zero due to density variations if fast dissolution or nucleation occurs [51].

In the case of homogeneous materials, it can be assumed that permeability depends on porosity. This relationship is expressed by the Kozeny-Carman law [10, 29]

$$K(\varepsilon) = K_0\frac{\varepsilon^3}{(1-\varepsilon)^2}, \tag{2}$$

so that the inverse permeability in equation (1) is $K(\varepsilon)^{-1} = K_0^{-1}(1-\varepsilon)^2/\varepsilon^3$, well defined and vanishing in pure fluid regions (*i.e.* where porosity equals 1). Moreover, permeabilities K and K_0 are scalar here, and feature isotropic samples and local rock matrix materials, but this formalism also applies in the case of a tensorial permeability.

In this formulation, porosity is a scalar field, potentially highly variable in space (and time). In particular, this model enables degeneration fo porosity to 1, modeling a pure fluid region, which locally results in the classical Stokes equation. In the context of pore-scale modeling, this formulation take into account both the fluid region inside the

pores and the (small) porosity of the surrounding matrix: it is a two-scale model. Furthermore, such a term can be used as a penalization technique in order to satisfy a no-slip condition at the fluid/solid interface [48, 3], by choosing a value of ε that is as small as possible (given the robustness of the numerical method used, since the problem becomes stiffer as ε decreases).

In the context of highly viscous Darciean flow, the first two terms of equation (1) are negligible. In combination with the Kozeny-Carman law (2) we therefore obtain:

$$-\mathrm{div}\,(\mu D(u)) + \mu^* K_0^{-1} \frac{(1-\varepsilon)^2}{\varepsilon^2} u = \varepsilon(f - \nabla p) \tag{3}$$

2.2. Velocity-vorticity model and boundary conditions

We can convert this expression into a velocity-vorticity formulation by taking the curl of equation (3) and introducing vorticity $\omega = \nabla \times u$:

$$-\mathrm{div}\,(\mu D(\omega)) + \nabla \times \left(\mu^* K_0^{-1} \frac{(1-\varepsilon)^2}{\varepsilon^2} u \right) = \nabla\varepsilon \times (f - \nabla p) \tag{4}$$

where the right hand side is neglected in the following, since the curl of the Kozeny-Carman term generates a $\varepsilon^{-3}\nabla\varepsilon$ term that is colinear to the right hand side but several orders of magnitude larger (in the purely fluid pore space, ε is constantly equal to 1 so the term vanishes, assuming $\nabla \times f = 0$). This needs to be supplemented with a Poisson equation that links velocity to vorticity:

$$-\Delta u = \nabla \times \omega \tag{5}$$

Let us consider that the driving force is along direction X, so that the sample is bounded in an impermeable non-reactive cell in directions Y and Z. This leads to the following boundary conditions, reflecting the experiments: In the computational Cartesian box Ω, the boundary conditions are periodic in directions Y and Z (the XZ and XY faces respectively), whereas $\partial u_x/\partial n = \partial p/\partial n = 0$ and $u_y = u_z = 0$ in the direction X (the YZ face).

These boundary conditions ensure that $\mathrm{div}\, u = 0$ on every face, along with

$$\Delta \mathrm{div}\, u = \mathrm{div}\,(\nabla \times \omega) = 0,$$

so that $\mathrm{div}\, u = 0$ everywhere (0 being the only solution of this equation). Velocity is lifted by a constant vector $\overline{u}e_x$, that controls the flow rate and make it possible to fit the correct driving force f by proportionality (using the linear feature of the DBS equation).

2.3. Reaction model

This velocity-vorticity formulation needs to be completed by the transport equation for the fluid species. Following the Quintard & Whitaker notation, the mass fraction and the molar mass of the k-th component are denoted $\overline{\omega}_{f,k}$ and M_k, respectively. Fluid density, which is assumed to be constant, is denoted by ρ_f, and the volume fractions of the solid and fluid phases are denoted by ε_f and ε_s, respectively. Both are related by

$$\varepsilon_f = \varepsilon = 1 - \varepsilon_s.$$

The mass balance by fluid species is then written [46, 51]

$$\begin{aligned} &\frac{\partial \varepsilon_f \rho_f \overline{\omega}_{f,k}}{\partial t} + \mathrm{div}\,(u \rho_f \overline{\omega}_{f,k}) \\ &\quad -\mathrm{div}\,(\varepsilon_f \rho_f \sigma_k(\varepsilon) \nabla \overline{\omega}_{f,k}) = \dot{m}_k \end{aligned} \tag{6}$$

where σ_k are the diffusion coefficients of the k-th species into the fluid. We introduce the superficial concentration

$$C_k = \varepsilon_f \rho_f \overline{\omega}_{f,k} / M_k \tag{7}$$

and the reaction rate $R_k(C) = \dot{m}_k/M_k$, so that the number of moles of the k-th species in a control volume V is $C_k V$ and its concentration by unit of fluid is C_k/ε_f. All concentrations can be stacked into a vector $C \in \mathbb{R}^N$, and the reaction rates into a vector $R(C)$ depending on the concentrations C_k (including the stoichiometric coefficients). Consequently, equation (6) can be rewritten as

$$\frac{\partial C_k}{\partial t} + \mathrm{div}\,(\varepsilon^{-1} u\, C_k) - \mathrm{div}\,(\sigma_k(\varepsilon) \nabla^\varepsilon C_k) = R_k(C) \tag{8}$$

and for the solid phase we obtain

$$\frac{\partial C_k}{\partial t} = R_k(C) \tag{9}$$

We assume that diffusion follows Archie's law [4] as expressed by Wakao & Smith [56] :

$$\sigma_k(\varepsilon) = \varepsilon D_M \tag{10}$$

where D_M is the molecular diffusion of the k-th component. In practice, the lifted operator $\nabla^\varepsilon = \varepsilon\nabla\varepsilon^{-1}$ can be approximated by the gradient operator ∇.

The boundary conditions for the concentrations are similar to those of the velocity: periodic on the lateral faces, since the non reactive cell prevents the chemical species from reaching these faces, and the input/output conditions in the direction X are given by a fluid buffer with an inlet value (Dirichlet boundary condition) and free exit.

2.4. Global system considered for calcite dissolution

In the context of the dissolution of a calcite body, occuring in carbonate rocks, the idealized chemical reaction considered here is given by

$$\mathrm{CaCO_3} + \mathrm{H^+} \rightleftharpoons \mathrm{Ca^{2+}} + \mathrm{HCO_3^-} \tag{11}$$

where species concentrations $C(x,t) \in \mathbb{R}^3$ are denoted by $C_1 = [\mathrm{CaCO_3}]$, $C_2 = [\mathrm{H^+}]$ and $C_3 = [\mathrm{Ca_2^+}] = [\mathrm{HCO_3^-}]$. Indeed, a synthetic case is considered in which the initial fluid is ideally free of $\mathrm{Ca_2^+}$ and $\mathrm{HCO_3^-}$, which leads to a permanent equality between these concentrations.

This spatially distributed reaction is modeled by the evolution of the superficial velocity (3) and concentrations (8)-(9) as follows:

$$\begin{cases} -\mu\Delta u + \mu K_0^{-1}\dfrac{(1-\varepsilon)^2}{\varepsilon^2}u = \varepsilon(f - \nabla p) \\ \dfrac{\partial C_1}{\partial t} = r(C) \\ \dfrac{\partial C_2}{\partial t} + \mathrm{div}\,(\varepsilon^{-1}u\,C_2) - \mathrm{div}\,(\sigma_k(\varepsilon)\nabla C_2) = r(C) \\ \dfrac{\partial C_3}{\partial t} + \mathrm{div}\,(\varepsilon^{-1}u\,C_3) - \mathrm{div}\,(\sigma_k(\varepsilon)\nabla C_3) = -r(C) \\ C_1 = (1-\varepsilon)/V_m \end{cases} \tag{12}$$

where $V_m = 36.93\mathrm{cm}\cdot\mathrm{mol}^{-1}$ is the molar volume of calcite.

The reaction rate, associated with an acid kinetic mechanism [18, 55], is given by the transition state theory (TST, [30, 53]), expressed as follows:

$$r(C) = -K_s A_s\left(1 - \frac{C_3^2}{K_{eq}C_1C_2}\right)\gamma_2 C_2 \tag{13}$$

where $\gamma_2 = 10^3\mathrm{cm}\cdot\mathrm{mol}^{-1}$ is the activity of $\mathrm{H^+}$. A consequence is that porosity follows the equation

$$\frac{\partial\varepsilon}{\partial t} = K_s A_s V_m\left(1 - \frac{V_m C_3^2}{K_{eq}(1-\varepsilon)C_2}\right)\gamma_2 C_2$$

3. Particle methods

3.1. Lagrangian formulation of (8)

Equations (8-9) can be solved based on a particle description of C:

$$\widetilde{C}_k(t) = \sum_p C_{k,p}(t)\delta_{\xi_{k,p}(t)}v_{k,p}(t) \tag{14}$$

where (C_p, ξ_p, v_p) are concentration-position-volume triplets, called particles, that are function only of time t.

Each species has its own particle description, since they can be transported at different velocities. Here we distinguish the fluid species from the solid species according to the velocity. The latter remains at rest, *i.e.* its velocity is equal to zero, which is compatible with equation (9).

From a theoretical perspective, the delta functions δ denote Dirac functions defined at different positions, including generalized functions suitable for the analysis. From a practical perspective, this can be understood as being the position of the particle.

The diffusion-transport equation (8) can be computed by means of a Lagrangian method, using the particle formulation (14). By means of an operator splitting between transport-diffusion on the one hand, and reaction on the other hand, the following system of equations is obtained:

$$\begin{cases} \dfrac{dC_{k,p}}{dt} = \left[\mathrm{div}\,(\sigma_k(\varepsilon)\nabla C_k) - C_k u\cdot\nabla\varepsilon^{-1}\right]_{\xi_{k,p}(t)} \\ \dfrac{d\xi_{k,p}}{dt} = \varepsilon^{-1}(\xi_{k,p}(t))u(\xi_{k,p}(t)), \\ \dfrac{dv_{k,p}}{dt} = \left[\mathrm{div}\,(\varepsilon^{-1}u)\right]_{\xi_{k,p}(t)}v_{k,p}(t), \end{cases} \tag{15}$$

so long as $\operatorname{div} u = 0$, so that

$$\operatorname{div}(\varepsilon^{-1} u\, C_k) = \varepsilon^{-1} u \cdot \nabla C_k + C_k u \cdot \nabla \varepsilon^{-1},$$

and such that the chain formula for the transport term $\varepsilon^{-1} u \cdot \nabla C_k$ leads to the dynamical system on the particle positions, pushed by the field $\varepsilon^{-1} u$, whose divergence controls the particle volume.

The only quantity that is of interest for reaction computations is the number of moles by unit of volume v_p, that is to say $C_{k,p} v_p$. This quantity satisfies

$$\begin{aligned} \frac{dC_{k,p} v_{k,p}}{dt} &= \frac{dC_{k,p}}{dt} v_{k,p} + \frac{dv_{k,p}}{dt} C_{k,p} \\ &= v_{k,p} \operatorname{div}(\sigma_k(\varepsilon) \nabla C_k)(\xi_{k,p}(t)) \end{aligned} \tag{16}$$

which is the same as if term $u \cdot \nabla \varepsilon^{-1}$ is removed from equation (15). Consequently, the set of equations (15) can be simplified to

$$\begin{cases} \dfrac{dC_{k,p}}{dt} = \left[\operatorname{div}(\sigma_k(\varepsilon) \nabla C_k)\right]_{\xi_{k,p}(t)}, \\ \dfrac{d\xi_{k,p}}{dt} = \varepsilon^{-1}(\xi_p(t)) u(\xi_{k,p}(t)), \\ \dfrac{dv_{k,p}}{dt} = 0. \end{cases} \tag{17}$$

The evaluation of $\operatorname{div}(\sigma_k(\varepsilon) \nabla C_k)$ on the particle positions $\xi_p(t)$ can be performed either by means of a Particle-Strength-Exchange method (a convolution with a diffusion kernel, cf. [44]), or using the usual cross-shaped scheme in which particles are dispatched on a uniform or structured grid. The positions $\xi_{k,p}(t)$ are obtained from a standard dynamical system that can be solved numerically using an explicit Runge-Kutta second- or fourth-order method, and whose solutions follow the field $\varepsilon^{-1} u$.

3.2. Remeshing and mesh transfers

When the DBS equation (3) and the reaction model (8)-(9) are combined to obtain the global reactive porous media system, a strong coupling is obtained between these equations: on the one hand the DBS equation (3) gives the superficial velocity field u and depends on porosity ε, and on the other hand the reactions give the porosity and depend on velocity (the fluid reactions (9) and the solid reactions (9) are coupled). The evolution of species concentrations in the fluid can be described either in a Eulerian way by (8) or in a Lagrangian way by equation (17).

In order to construct an efficient solution scheme, the DBS equation can be solved using a method (finite elements, finite volumes, finite differences, etc.) other than the one used for the reaction equation, for which a Lagrangian framework is adopted in this study. These different formulations do not need to be simulated at the same resolution. However, whatever the method chosen to solve the DBS equation, the particle position $\xi_{k,p}(t)$ of the fluid species will generally not coincide with the points/nodes of the DBS discretization, nor with the particle positions of the solid species. Consequently, the solid chemical species $C_{k,p}(t)$, need to be interpolated on the grid used for solving the DBS equation (in order to obtain ε) and on the fluid particles (in order to obtain the diffusion coefficients). Furthermore, the velocity has to be interpolated to the Lagrangian set of particles so that u is available for solving equations (17). In addition, it is imperative to periodically re-position the particles on a structured lattice in order to avoid regions with too much or too little information. This is particularly important around stagnation points. The interpolation procedure is called remeshing and is crucial to ensure the accuracy and the convergence of particle methods.

Interpolation and remeshing are performed by means of convolution with strongly compact-supported kernels. Let us consider a generalized function:

$$F = \sum_p F_p \delta_{x_p} v_p$$

defined in a point-wise manner at positions $x_p \in \mathbb{R}^d$, another set of positions $\widetilde{x}_q$, and a kernel $K : I \to \mathbb{R}$ where I is an interval centered on 0.

The interpolation from a set of points to another is then defined by the convolution

$$\begin{aligned} \widetilde{F}_q = F * K_h(\widetilde{x}_q) &= \int_{\mathbb{R}^d} F(y) K_h(\widetilde{x}_q - y) dy \\ &= \sum_p F_p K_h(\widetilde{x}_q - x_p) v_p, \end{aligned} \tag{18}$$

where K_h is the rescaled kernel defined by

$$K_h(x) = \frac{1}{h^d} K^{\otimes d}\left(\frac{x}{h}\right) = \frac{1}{h^d} K\left(\frac{x_1}{h}\right) \dots K\left(\frac{x_d}{h}\right), \tag{19}$$

whose characteristic length h is the typical distance between particles. In the event of interpolation on a structured grid, this length is naturally the step size, possibly generalized to anisotropic grids (different values of h depending on the direction).

The integral of kernel K must be equal to 1 in order to ensure a consistent interpolation. Moreover, it must satisfy zero-momentum up to the order p:

$$\int_{-\infty}^{\infty} K(z) z^k dz = 0 \quad \text{for all } k = 1..p \tag{20}$$

with the $(p+1)$-th momentum bounded [40].

In order to achieve the best possible interpolation/remeshing, it is necessary to maximize the order and the regularity of K. However, K is either of order 1 and relatively inaccurate (but consistant), or is at least order 2, and the second momentum at zero implies that K is negative, meaning that the sign of the interpolated quantity is not preserved. This point is especially problematic in the case of chemical computations.

Among the symmetric kernels considered in the present work, one can mention

$$M_4(x) = \begin{cases} (2-x)^3/6 - 2(1-x)^3/3 & \text{if } 0 \le x \le 1 \\ (2-x)^3/6 & \text{if } 1 \le x \le 2 \\ 0 & \text{if } x \ge 2, \end{cases} \tag{21}$$

which is of order 1 (cf. [11]) but more regular than the "hat" or "tent" function $\Lambda_g(x) = [1-x]^+$, and

$$M_4'(x) = \begin{cases} (3x^3 - 5x^2 + 2)/2 & \text{if } 0 \le x \le 1 \\ (2-x)^2(1-x)/2 & \text{if } 1 \le x \le 2 \\ 0 & \text{if } x \ge 2, \end{cases} \tag{22}$$

which is of second order and of class C^3 except in 0 (see [40] and [12, 13]). A variant of M_4 with a shorter support is

$$M_3(x) = \begin{cases} 3/4 - x^2 & \text{if } 0 \le x \le 1/2 \\ (3/2 - x)^2/2 & \text{if } 1/2 \le x \le 3/2 \\ 0 & \text{if } x \ge 3/2, \end{cases} \tag{23}$$

Moreover the preservation of the discrete integrals is ensured by the spline-like property of all these kernels Λ_g, M_3, M_4 and M_4':

$$\sum_{j \in \mathbb{Z}} K(x + j) = 1. \tag{24}$$

This can easily be demonstrated in 1D, but the demonstration being is in any dimension by using the tensorial writing of the kernel (19). Indeed, if the receiving particles are located on a structured grid, that is $\widetilde{x}_q = qh$ and $\widetilde{v}_q = h$ for all $q \in \mathbb{Z}$, then the interpolation formula (18) reads

$$\begin{aligned} \sum_q \widetilde{F}_q \widetilde{v}_q &= \sum_q \sum_p F_p K_h(\widetilde{x}_q - x_p) v_p \widetilde{v}_q \\ &= \sum_p F_p v_p \sum_q K_h(qh - x_p) \widetilde{v}_q \\ &= \sum_p F_p v_p \sum_q K(q - x_p/h) = \sum_p F_p v_p \end{aligned} \tag{25}$$

which ensures mass conservation when applied to the species concentrations, and momentum conservation when applied to velocity fields.

3.3. Evidence of over-diffusion effects

In addition to the issues related to sign-preserving, another potential issue is over-diffusion. A first indication is that $M_3(0) = 3/4 \neq 1$ and $M_4(0) = 2/3 \neq 1$. More precisely, it can be shown that on a structured grid there exists a quadrature of the Laplace operator Δ_h such that the convolution by one of these kernels is expressed as $1 - \beta h^2 \Delta_h + O(h^3)$ with $\beta \geqslant 0$.

To show how this over-diffusion can be corrected and quantified it, a one-dimensional configuration is described. Let us consider a uniform grid $x_p = ph$, $p \in \mathbb{Z}$ on which particles are positioned. If we consider the usual second order finite difference scheme

$$u''(x_p)h^2 = -u(x_{p-1}) + 2u(x_p) - u(x_{p+1}) + O(h^4),$$

and the Radon measure (pointwise description)

$$d\xi = h \sum_{p \in \mathbb{Z}} d\delta_{x_p},$$

it is easy to show that

$$u * K(x_p) = u(x_p) + K(1)h^2u''(x_p) + O(h^4). \tag{26}$$

The diffusion induced by the remeshing process is therefore

$$D_R = K(1)h^2/\delta t \tag{27}$$

when formalized as an explicit Euler scheme whose time step is denoted δt.

The correction across several dimensions of space is the same the one dimensional correction, each 1D correction acting on one second derivative of the Laplace operator. Indeed, in two variables of space, with step sizes δx and δy, the equation (26) is written

$$\begin{aligned} u * K^{\otimes 2}(x,y) &= \int_{\mathbb{R}}\left(\int_{\mathbb{R}} u(x-\xi_1, y-\xi_2)K(\xi_1)d\xi_1\right)K(\xi_2)d\xi_2 \\ &= \int_{\mathbb{R}}\left(u(x,y-\xi_2) + K(1)\delta x^2\frac{\partial^2 u}{\partial x^2}(x,y) + O(\delta x^4)\right)K(\xi_2)d\xi_2 \\ &= u(x,y) + K(1)\delta x^2\frac{\partial^2 u}{\partial x^2}(x,y) + K(1)\delta y^2\frac{\partial^2 u}{\partial y^2}(x,y) + K(1)^2\delta y^2\delta x^2\frac{\partial^4 u}{\partial x^2\partial y^2}(x,y) + O(\delta x^4) + O(\delta y^4) \end{aligned} \tag{28}$$

This is easily generalized to multi-dimensional remeshing, which gives, assuming that a common step size h is used:

$$u * K^{\otimes d} = u + K(1)\, h^2\Delta u + O(h^4), \tag{29}$$

leading to the same correction coefficient given by equation (27). In case of different step sizes, one can either rescale the kernels differently (depending on the direction) or use this result to apply an anisotropic correction to the diffusion.

Despite the fact that there is no stability condition due to the $1/\delta t$ term, artificial diffusion can be critical in digital rock physics simulations, which typically use values of h that are much larger compared to the characteristic dimensions (of pores for example).

We will use the following example to illustrate our approach, designed to tackle this over-diffusion problem. Let us consider the interval $\Omega = [-\pi, \pi] \subset \mathbb{R}$, on which periodic boundary conditions are imposed, such that $h = 2\pi/N$ and the nodes are $x_p = -\pi + ph$ with $p = 0..N-1$. Let us further assume that the porosity is 1% in the interval $[1, 2]$ and 100% elsewhere. The diffusion coefficient follows the discontinuous Archie's law $\sigma(x) = \sigma_0\varepsilon(x)$ with $\sigma_0 = 0.5$. The numerical parameters are $N = 100$ and $\delta t = 10^{-2}$, and the initial condition is given by the one-dimensional Gaussian function $G(x, 1/2)$ with

$$G(x, s) = \frac{1}{s\sqrt{2\pi}}e^{-x^2/2s^2} \tag{30}$$

here denoted without subscript since there is only one component in this example, consequently defining the initial values of particle $C_p(0) = G(x_p, 1/2)$.

This diffusion equation, the solution to (17) with a velocity of zero, is solved by means of a second order Implicit Euler scheme and displayed as a plain black line in Figure 1 at different times. The initial condition is displayed as a dashed line. It can be observed that if the porosity were constant, the exact solution would be

$$C(x,t) = G(x, \sqrt{s^2 + 2\varepsilon t}), \tag{31}$$

but the fact that the porosity drops from 1 to 10^{-2} in the interval $[1, 2]$ generates a slope discontinuity, making this example a non-trivial test case.

Solving the same test case using alternate diffusion and remeshing steps with kernel M_4 yields the solution represented by red "+" symbols. Over-diffusion, suggested by formula (26), leads to substantial lack of accuracy, especially when computing the boundary layer in the low porosity domain.

3.4. A posteriori adaptive kernels

In the present work we propose to perform an *a posteriori* kernel selection based on the local Peclet number, as opposed to an *a priori* kernel selection.

It is easy to demonstrate that *a priori* selective interpolation is not suited to this family of kernels. To do so, a formula (18) is generalized to a space-dependent kernel $\Lambda(y, \cdot)$ such as

$$\widetilde{F}(x) = \int_{\mathbb{R}^d} F(y)\Lambda^h(y, x-y)dy, \tag{32}$$

where $\Lambda^h(y,z) = h^{-d}\Lambda(y, z/h)$ and $\Lambda(y,\cdot)$ is M_4' if $y \leq 0$ and M_4 if $y > 0$. If we consider the constant pointwise function over $\mathbb{R}$ equal to $a \in \mathbb{R}$ defined by

$$F = \sum_{k\in\mathbb{Z}} a\delta_{kh}h, \tag{33}$$

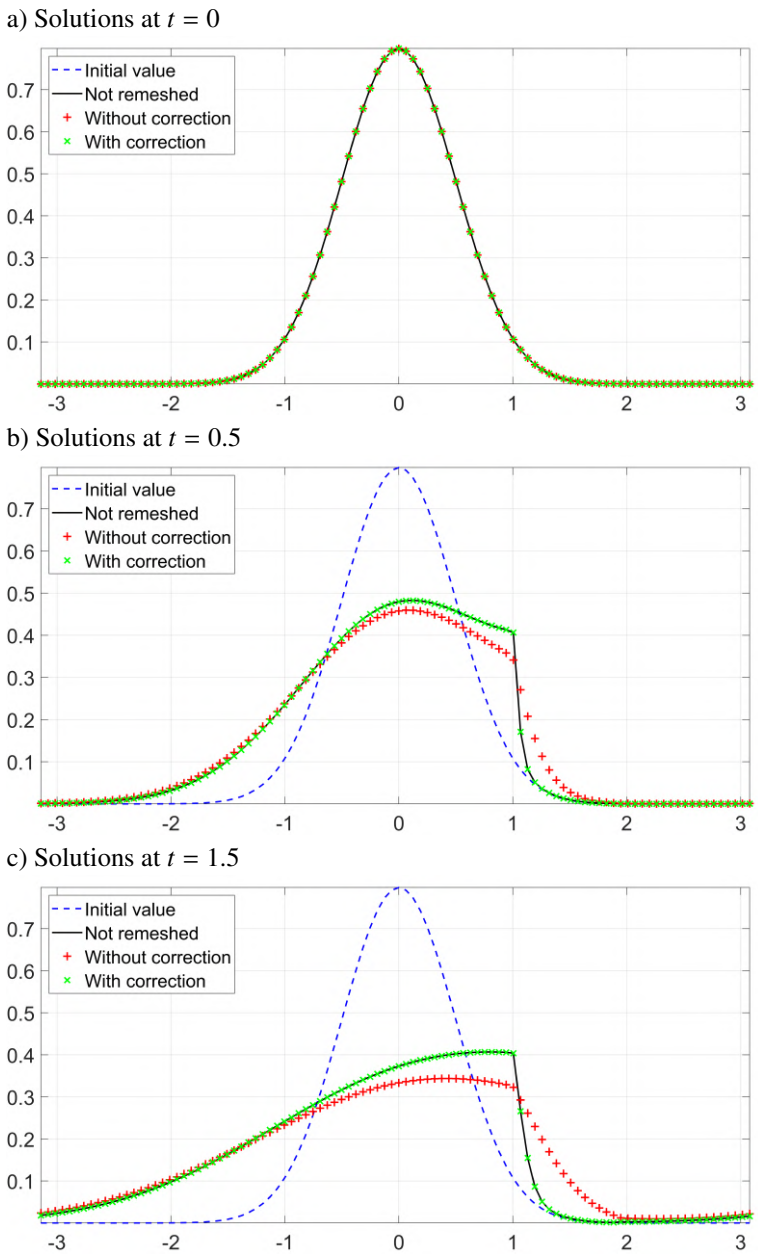

Figure 1: Solutions at $t = 0, 0.5$ and 1.5 of a 1D diffusion equation using remeshing in a porous medium with variable porosity (the porosity is 1% in the interval $[1, 2]$ and 1 elsewhere), whose initial condition is a Gaussian function (- -). The solutions are obtained with (××) and without (++) correction, and the reference solution is the non-remeshed simulation (—).

then its 1D remeshed value at 0 is given by

$$\begin{aligned} \widetilde{F}(0) &= a\Lambda(-1,-1) + a\Lambda(0,0) + \Lambda(1,1) \\ &= aM_4'(-1) + aM_4'(0) + aM_4(1) = \frac{7}{6}a \end{aligned} \tag{34}$$

which is unstable when performing successive steps of remeshing (as a geometric sequence).

Consequently, an *a posteriori* selective kernel is introduced. The proposed strategy for choosing the kernel is motivated by the following observation: the second order kernel M_4' is not diffusive and can be used when the particle motion is limited, namely when the distance traveled in one time step is close to 0.

This is typically quantified by the local Courant-Friedrich-Lewy value $\alpha(x) = u(x)\delta t/h$, which implies the definition of the slow region by:

$$\Omega_{slow} = \left\{x \in \Omega : \alpha(x) < \alpha_0\right\} \tag{35}$$

for a given threshold $\alpha > 0$. It is then possible to select the kernel required to perform an *a posteriori* interpolation, switching from a kernel Λ_1 in the slow region to a kernel Λ_2 elsewhere by means of the formula:

$$\widetilde{F} = \mathbf{1}_{\Omega_{slow}} F * \Lambda_1 + \mathbf{1}_{\Omega_{fast}} F * \Lambda_2 \tag{36}$$

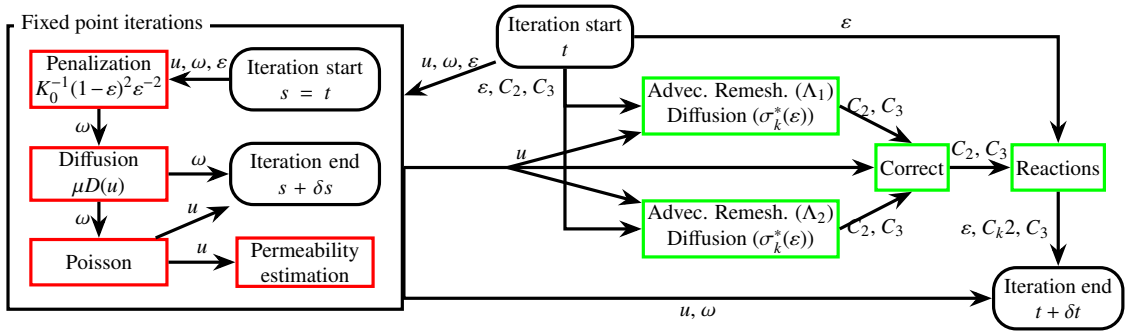

Figure 2: Directed acyclic graph for 2D and 3D numerical examples. Squared nodes represent operators, rounded nodes represent terminal nodes. Red and green operators are applied on CPU and GPU targets. The left part of the diagram describes the operator sequence for numerically solving the DBS equation, and the right part describes the numerical method used for the chemical convection-diffusion-reaction equations. In the present applications, the two remeshing kernels are $\Lambda_1 = M_4$ and $\Lambda_2 = M_4'$.

where $\Omega_{fast} = (1 - \mathbf{1}_{\Omega_{slow}})$, $\mathbf{1}$ being the characteristic function of the set denoted in the index.

When considering a low permeability medium, or when applying the Kozeny-Carman law (2), the superficial velocity of equation (3) scales as $\varepsilon^2\sqrt{K_0}$ (the boundary layer scales as $\varepsilon\sqrt{K_0}$ with the right-hand-side scaling as ε). This means that the slow region, owing to the Archie's law, is also the region of the weakest species diffusion. When applying the remeshing procedure, it is consequently a good strategy to:

- Use a non diffusive kernel in the slow region, whose lack of sign preservation will not affect particles at quasi-rest,
- Use a sign-preserving kernel in the fast region, whose diffusion D_R can be predicted and used to correct the diffusion coefficient $\sigma_k(\varepsilon)$.

In practice, we will apply formula (36) with M_4 in the fast region and M_4' in the slow region:

$$\widetilde{F} = \mathbf{1}_{\Omega_{slow}} F * M_4' + \mathbf{1}_{\Omega_{fast}} F * M_4 \tag{37}$$

in combination with the corrected diffusion coefficient

$$\sigma_k^*(\varepsilon) = \sigma_k(\varepsilon) - \mathbf{1}_{\Omega_{fast}} M_4(1) h^2/\delta t \tag{38}$$

The correction term is the d-dimensional equivalent of equation (27) for the diffusion induced by remeshing with kernel M_4. It can be observed that this correction is evaluated by means of particles at rest, inducing the value $M_4(1)$. This may be improved by considering the local topology of the particle network, but at the cost of a great deal of computational time. The present solution has no computational cost, and is shown (see section 5.1) to already dramatically improve the convergence of the method.

4. Computational aspects and GPU implementation

4.1. Numerical method

The transport-diffusion-reaction equations are solved by the Lagrangian method (17) described above, including the correction (37)-(38), and the resulting dynamical system is solved by a Runge-Kutta fourth-order method. At each sub-step, its velocity field can be obtained by solving the Darcy-Brinkman-Stokes equation in its formulation (4).

After introducing the vorticity $\omega = \nabla \times u$ and the operator

$$\mathcal{A}^u v = \nabla \times (2D(u)v) - \Delta u \times v,$$

we can see that

$$\nabla \times \operatorname{div}(2\mu D(u)) = \mathcal{A}^u \nabla\mu + \mu\Delta\omega.$$

For a constant viscosity μ, $\mathcal{A}^u\nabla\mu \equiv 0$, so the solution of the DBS equation is obtained as the limit of the following sequence:

$$\widetilde{\omega}^{n+1} - \omega^n - q\mu\Delta\widetilde{\omega}^{n+1} + q\nabla \times \left(\mu^* K_0^{-1} \frac{(1-\varepsilon)^2}{\varepsilon^2} u^n\right) = 0 \tag{39}$$

where q is a descent parameter whose dimension is a mass per unit of time, with the boundary conditions mentioned in section 2. The consistency of this fixed-point method, is discussed in [24]. In the event of variable viscosity,

this method can be easily generalized by adding the source term $\mathcal{A}^{u^n}\nabla\mu$. The velocity at the next time step is then recovered either by

$$-\Delta u^{n+1} = \nabla \times \widetilde{\omega}^{n+1}, \tag{40}$$

or by

$$-\Delta \psi^{n+1} = \widetilde{\omega}^{n+1} \quad \text{followed by} \quad u^{n+1} = \nabla \times \psi^{n+1}, \tag{41}$$

including the lift velocity at the boundary conditions providing the driving force. These sequences, (39)-(40) or (39)-(41), are always evaluated after a remeshing step, so that all the differential operators are computed by straightforward finite difference schemes (fourth-order), since the remeshed particle network is structured. These last three equations are implicit and involve non-separable Poisson equation, solved fusing the MudPack solver based on Fast Fourier Transforms (FFT) and Tchebitchev polynomials [1]. These algorithms complexity scale as $O(n \log n)$ where n is the number of particles (coinciding with the number of underlying grid points of the remeshed particle network). For more details, see [23, 14, 38, 16] for the velocity-vorticity formulation and [48, 12] for the velocity-pressure formulation.

Remeshing and finite difference schemes are processed direction by direction [36], which corresponds to a second level of fractional steps algorithms. In the present simulations, we use the sequence (39)-(41), whose numerical solution algebraically satisfies:

$$\operatorname{div} u^{n+1} = \operatorname{div}(\nabla \times \psi^{n+1}) = 0,$$

since the discrete operators of finite difference schemes satisfy $\operatorname{div}(\nabla\times\cdot) \equiv 0$ exactly. Note that to satisfy this property for the sequence (39)-(40) staggered grids are required, but by using colocation the state variable is aligned with the microCT scan data.

Once the velocity has been updated, the chemical system (17) in its Lagrangian form is pushed to the next time step by means of a Runge-Kutta second- or fourth-order scheme, diffusion is computed by a finite difference scheme. As mentioned above, an important consequence of the Lagrangian formulation is that it removes the transport terms in equation (17), hence removing as well its stability condition, leading to aparticularly robust method. Lastly, the resulting particles carrying the chemical state variable are remeshed on the underlying uniform grid, which has no impact on the divergence free velocity field, and the next time step can begin. Figure 2 shows the directed acyclic graph for these temporal iterations.

4.2. Hybrid CPU-GPU implementation

The numerical applications presented below where performed using an in-house code, which is due to be being open source and is currently in its first release candidate version. The software is a generic high-performance hybrid computing code for remeshed particle methods.

The entire code is based on an operator splitting strategy where each operator is solved with the most appropriate numerical method. Currently, all the methods considered are Cartesian grid based methods such as finite difference, spectral and remeshed particle methods. The actual development started with the introduction of high-order remeshing formulas, well-suited to GPU implementation using OpenCL [17, 13]. More recently, the code has been successfully used for passive control of bluff body flows [37] and for sediment flow simulations [26]. In the next paragraphs we briefly describe the key features of the library.

The overall structure of the library is written in Python so as to benefit from object-oriented programming and high-level interfaces with utilities such as data representation on cartesian grids, MPI, OpenCL, compiled languages interoperability, symbolic computations, and HDF5 parallel I/O through the Python packages `numpy`, `mpi4py`, `pyOpenCL`, `f2py`, `sympy` and `h5py`.

Using the code consists in defining the different operators that act on several variables defined on a computational domain. The operators are obtained by equations splitting. The variables are either present in the equations or intermediate variables. This high level of abstraction is designed to solve problems regardless of the architecture and discrete models used. In practice, the problem description must be formalized as a directed acyclic graph of operators that defines a temporal iteration of the semi-discrete equations where vertices represent the operators and edges represent the dependencies between operators. Operators are defined along with their numerical discretization, numerical method parameters and targeted architecture. The graph is automatically completed in order to insert appropriate low level operators and ensure data consistency of variables across the different discretization characteristics and architecture.

Once the graph is defined, the GPU targeted operators are being initialized by means of automatic code generation and performance auto-tuning. GPU kernels code is generated either using simple text formatting capabilities or abstract syntax trees from a symbolic representation of variables. The former is used in case of complex algorithms generated by numerical methods, while the latter is mostly used for vectorization of simple expressions. The autotuning of the GPU kernels ensures optimal use of resources thanks to the adjustment of kernel parameters with discretization and hardware capabilities.

Finally, data locality is managed automatically in the case accelerated and distributed architectures. GPU operators work on device-mirrored data, and memory coherence is maintained by the library itself thanks to the `pyOpenCL` package. Distributed architectures are handled by a fixed domain decomposition through MPI cartesian topologies. All communication patterns can therefore be set up and optimized during the initialization phase.

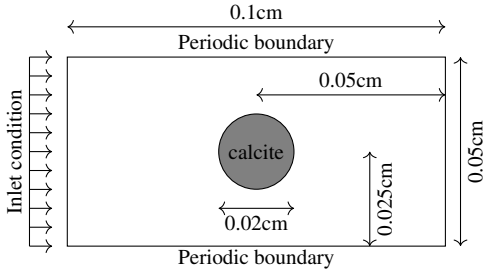

Figure 3: 2D validation benchmark configuration .

Parameter	Symbol	Value	Units
Dynamic viscosity	μ	10^{-3}	$\mathrm{Pa} \cdot \mathrm{s}$
Kozeny-Carman permeability	K_0	10^{-10}	m^2
Inlet velocity	u_∞	2×10^{-5}	$\mathrm{m} \cdot \mathrm{s}^{-1}$
Molecular diffusion	D_M	10^{-12}	$\mathrm{m}^2 \cdot \mathrm{s}^{-1}$
Reaction velocity	K_s	10^{-2}	$\mathrm{m} \cdot \mathrm{s}^{-1}$
H^+ activity	γ_{H^+}	10^3	$\mathrm{cm}^3 \cdot \mathrm{mol}^{-1}$
Specific reactive area	A_s	1582	m^{-1}
Inlet acid concentration	C_{H^+}	10^{-2}	$\mathrm{mol} \cdot \mathrm{L}^{-1}$

Table 1: 3D carbonate rock dissolution parameters. Chemical constants are taken from [38], except for the specific area which is estimated by meshing the fluid-solid interface.

5. Application to rock dissolution

5.1. Validation of the fully coupled model

To validate the proposed model, the chemical reaction and the global model described in section 2.4 are considered, based on the 2D benchmark described in [38]. It consists of a circular 1% porous calcite core of radius 0.01cm in a channel 0.05cm wide and 0.1cm long, as shown in Figure 3, exposed to hydrochloric acid injection at $pH = 2$ and flow rate $0.12\mathrm{cm} \cdot \mathrm{s}^{-1}$. Periodic boundary conditions are set at the top and bottom walls, which by symmetry are equivalent to free slip and no-slip-through boundary conditions, for both the hydrodynamics and the species transport (including acid and products).

In Figures 4.a and 4.b we compare the spatial distribution of the acid concentration at two points in time for diffusive (top half) and diffusion-corrected simulations (bottom half). The most obvious difference is that the concentration gradient is spread out over a larger distance in the diffusive case. A closer look shows that the contour of the crystal is also slightly different, *i.e.* more elongated relative to the direction of flow in the corrected case.

Grain size evolution, defined as the volume inside the 0.5 level of porosity, is represented in Figure 4.c. It is clear that the simulations based on adaptive *a posteriori* kernel selection and a corrected diffusion coefficient yield similar results on all considered the meshes considered, predicting the time of complete dissolution at around $t = 4,200$ in accordance with results from [38]. Even on the finest discretization considered, the simulations using diffusive remeshing overestimate the time needed for complete dissolution.

Moreover, comparison of the contour at $t = 45$ min with the contours from [38] in Figure 4.d shows that the grain shape (isovalue at $\varepsilon = 0.5$) is quite similar, whether we use the corrected method (in blue) or not (in light green). The practical advantages of correction are, consequently, to avoid the appearance of fuzzy solid (see Figure 4.c for instance), to increase reliability since convergence is much improved when using the correction (the curves at 128×256 and 256×512 are superimposed in Figure 4.c). It is also worth noting that the present method does not need to be constrained by the reaction to be located at the interface, as it is commonly performed in dissolution simulations.

5.2. Dissolution of a non-percolating 3D carbonate rock

The second case focuses on the impact of dissolution on the hydraulic properties of carbonates. The rock studied is Indiana Limestone, an almost pure outcrop rock composed of 99% calcite. The initial geometry of the rock is provided by Ferreira et al. through the digital rocks portal [19, 20]. Based on the methodology outlined in Arns et al. [5] (the concept of backgroud porosity), Ferreira et al. argue that none of the voxels are pore-free at the resolution used. They conclude in a 5% porosity for the solid matrix, which is fully compatible with the present formalism, by setting $\varepsilon = 0.05$ in the solid region. This type of sample is especially challenging as it comprises both pores and a porous, but non-percolating, rock matrix. By non-percolating, we mean that the pure fluid region ($\varepsilon = 1$) is not

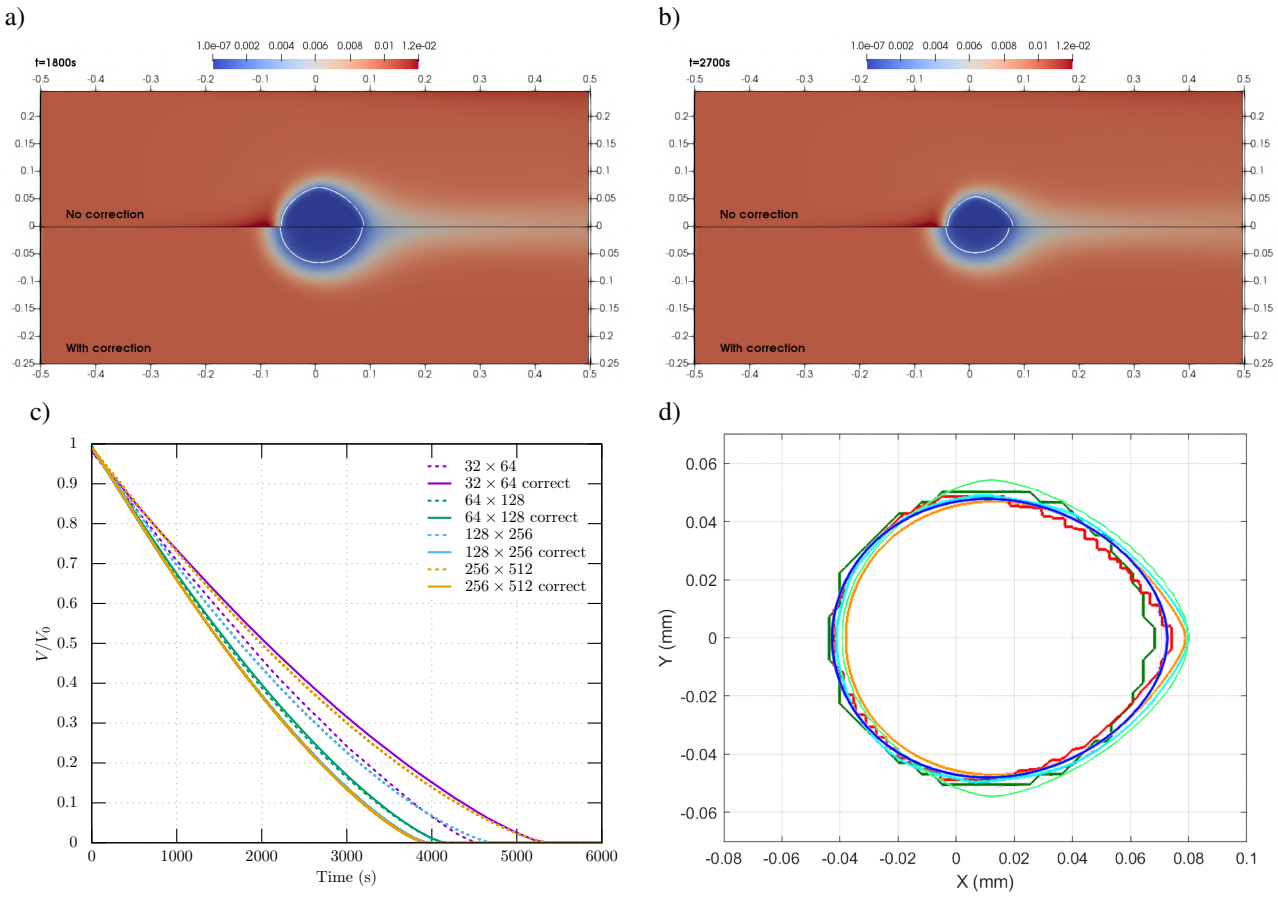

Figure 4: Correction according to $\varepsilon < 1.01\%$ criteria when applied. Top: Acid concentration C_{H^+} at $t = 1,800$ (a) and $t = 2,700$ (b) and $\varepsilon = 0.5$ contour (in white). The top halves represent the solution computed without correction; the bottom halves the corrected solution. Bottom left (c): Convergence of grain size evolution ($\int \mathbf{1}_{\varepsilon<0.5}$) for several resolutions without correction (dashed lines) and with correction (plain lines). Bottom right (d): Comparison of the contours obtained using the method without correction (light green) and with correction (in blue) with the contours obtained from [38] by other methods (cyan is Chombo-Crunch, orange is disolFOAM, red is OpenFOAM-DBS, dark green is lattice-Boltzmann).

continuous between the inlet and outlet faces. In this work, the gray level G of each voxel is converted into a porosity field ε as follows:

$$\varepsilon = \begin{cases} 1 & \text{if } 1 \leq G < G_{pt} \\ (1-0.05)\left(\dfrac{G_{ts}-G}{G_{ts}-G_{pt}}\right)^{\alpha} + 0.05 & \text{if } G_{pt} \leq G < G_{ts} \\ 0.05 & \text{if } G_{ts} \leq G \leq 2^{16}, \end{cases} \tag{42}$$

where the grey-level thresholds between the pores and the transition zone ($G_{pt} = 9,000$), and between the transition zone and the solid phase ($G_{ts} = 12,000$) are visually determined based on an image analysis, and where the exponent $\alpha = 2.25$ is calibrated such that the overall porosity of the rock corresponds to the measured porosity of 14.9% [19, 20].

The initial geometry is characterized by an absolute permeability of $K = 10^{-14}\text{m}^2$. The specific reactive area is computed from an estimation of the pore-solid interface so that $A_s = 1,582\text{m}^{-1}$. The other simulation parameters are summarized in table 1.

In this example, the following Péclet and Damköhler numbers are considered:

$$Pé = \frac{u_\infty \sqrt{K}}{D_M} = 2 \quad \text{and} \quad Da_{II} = \frac{r}{D_M A_s} = 6.3\,10^6, \tag{43}$$

and are expected to lead to wormhole formation [51].

The goal of the present study is to measure permeability evolution throughout the dissolution process. So several macroscopic indicators were computed as shown in Figure 7. We first computed a porosity estimate $\widetilde{\phi}$ of our sample based on the pores volume as

$$\widetilde{\phi} = \int_\Omega \varepsilon dv.$$

The estimation of the permeability $\widetilde{K}$ is derived directly from the Darcy's law as:

$$\widetilde{K} = \mu \langle u_x \rangle / f \tag{44}$$

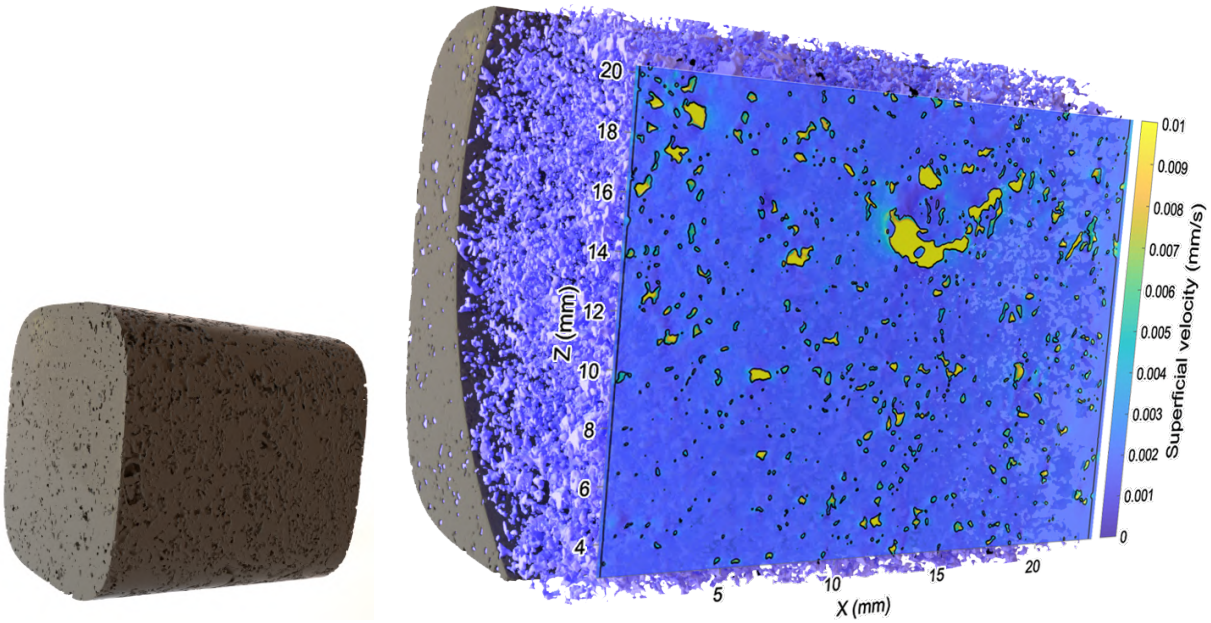

Figure 5: Rock sample of size 23.173mm. Left: body shape. Right: partial view of the body shape in the background, pore topology sliced with the superficial velocity.

where $\langle\cdot\rangle$ is a volume averaged quantity and u_x is the velocity in the flow direction. The term $f = \langle f - \nabla p\rangle$ (since $\langle\nabla p\rangle = 0$) is not computed in the method because of the velocity-vorticity formulation of the DBS equation (4). Consequently, we reconstructed this quantity through equation (8) from the computed values of u_x with second order finite differences.

One can see that if the fluid region Ω_{fluid} is defined where $\varepsilon = 1$ and $\varepsilon \to 0$ elsewhere. Hence considering a fluid/solid partition, then $\widetilde{\phi}$ tends towards the volume of Ω_{fluid} and u tends towards 0 in the solid region, so that the usual definition of permeability is obtained:

$$\lim_{\varepsilon\to 0} \widetilde{K} = \frac{\mu\widetilde{\phi}}{f} \int_{\Omega_{fluid}} u_x dv$$

Finally, the following averaged quantities $\langle C_2\rangle$ and $\langle C_3\rangle$ where also computed indicating the overall behavior of the chemical species.

From the raw dataset we extracted a sample of 512^3 voxels placed in a non-reactive and non-permeable solid casing. This region, denoted Ω, is defined as a quartic cylinder of radius 11mm in direction X, as shown in Figure 5. The choice of using a casing was made to improve the regularity of the geometry of domains to maximize the useful volume of data. The sample was taken at the same resolution as the raw data *i.e.* voxels of size 0.04526^3mm^3. Based on the sample data, an estimated porosity value of 15.6% was obtained which is close to the global rock porosity. After the first iteration of the method, the initial flow field was characterized and an averaged velocity in direction X of $\langle u_x\rangle = 2.045\,10^{-5}\text{m}\cdot\text{s}^{-1}$ was measured which corresponds to a mass flow rate of $10.981\text{mL}\cdot\text{s}^{-1}$. An initial permeability of $\widetilde{K} = 2.62\,10^{-14}\text{m}^2$ was obtained based on an estimation of the driving force of $f = 7.80\,10^5\text{Nm}^{-3}$ which is in a good accordance with the overall absolute permeability. This value may be sensitive to the choice of gray scale conversion (42) from microCT images.

In order to simulate the effect of fluid inclusions - what Gray et al. [21] refer to as detailed structure versus the homogeneous equivalent material - we focused on a sub-sample of 128^3 voxels that is characterized by the presence of a large pore in a crescent shape as illustrated in Figure 6. In this sub-sample we enforced boundary conditions inherited from the superficial velocity of the full sample, and began the simulation at $t = 0$ with the acid inlet at $pH = 2$ as for the full sample. As expected for the Péclet-Damköhler regimes, the acid flows created a dominant wormhole through the calcite connecting high porosity regions.

As shown in Figure 7.a, the dissolution process leads to an increase in porosity over time. A dramatic change occurs once the first wormhole reaches the opposite end of the sample material. The acid flow fills the opened pores and digs through the calcite in the regions with the lowest local porosity. As a result, the overall acidity rises over time, as shown in Figure 7.b. The sample considered contains a large, open, regular-shaped pore that explains the nearly constant evolution of products concentration during digging times. Once the dominant wormhole becomes a through hole, jumps in both permeability and concentration can be observed. When the wormhole is complete, the acid is expected to no longer be fully consumed, according to [20].

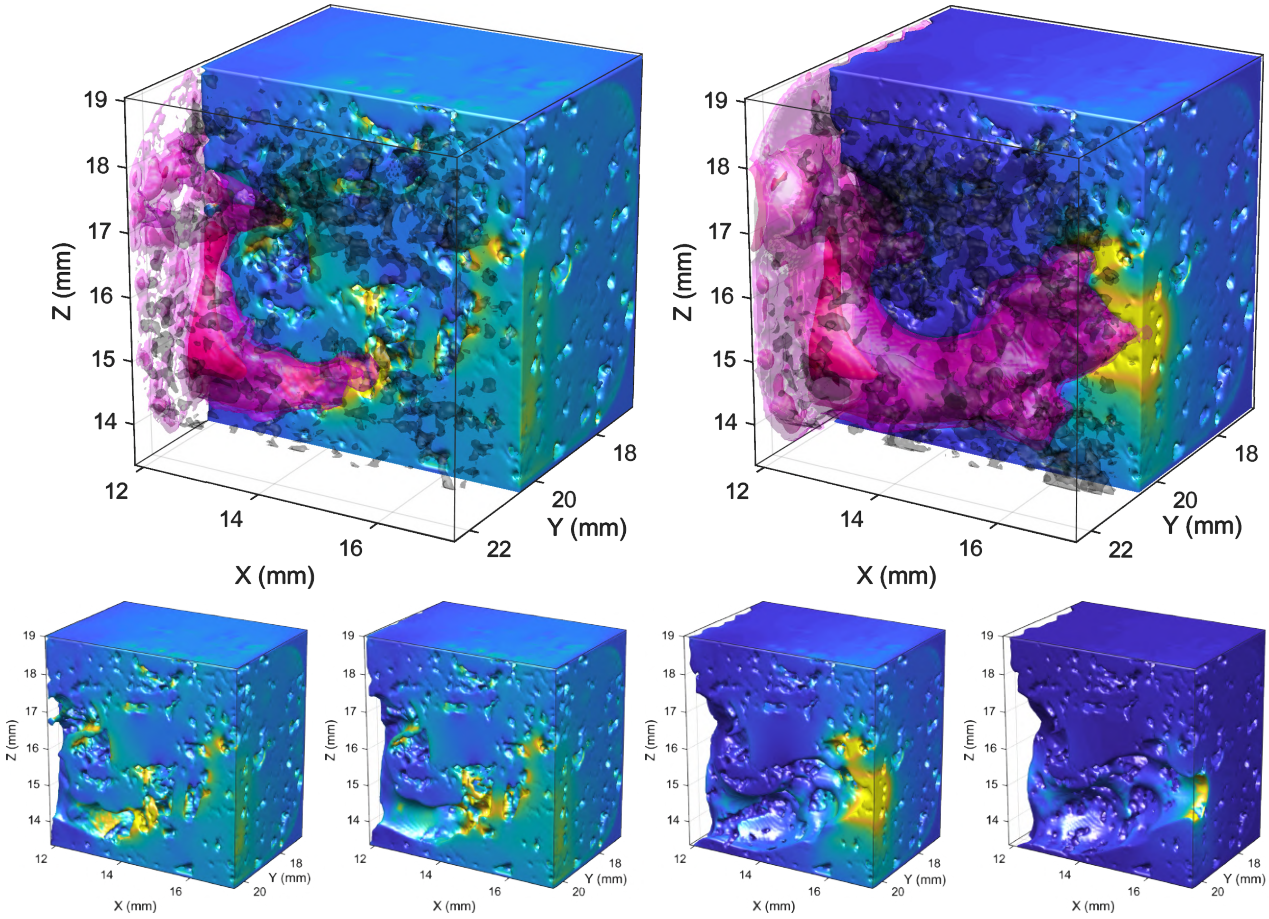

Figure 6: Pore connection obtained by acid perforation. Top: Rock sub-sample at initial time (to the left) and $t = 71h$ (to the right), colored by the superficial velocity, together with acid and product isosurfaces. Magenta surfaces correspond to isovalues of acid concentration at $pH = 2, 3$ and 4, respectively from the least to the most transparent surfaces, while black surfaces are isovalues of the product $C_3 = [HCO_3^-]$ at a concentration of 10^{-3}. The box location is around $X = 15$mm, $Z = 16$mm, and $Y = 3$mm, (a size of 5.79mm in each direction), sliced at 65% of the sub-sample in the Y direction. The dominant pore corresponds to the yellow structure in Figure 5 (highest velocity). To the bottom: snapshots of rock matrix at times t =1.3h, 14h, 71h and 103h (from left to right).

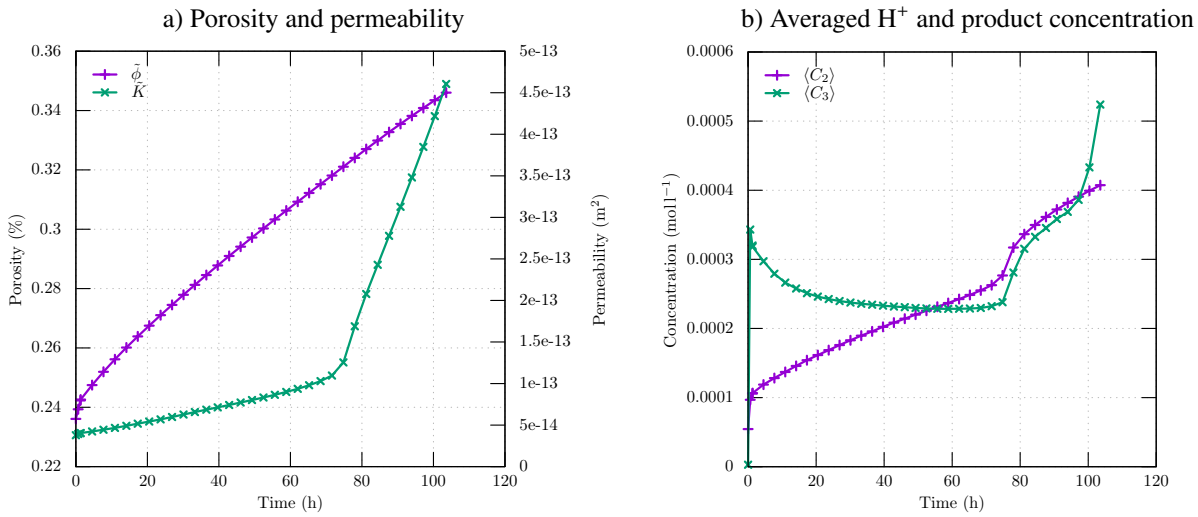

Figure 7: Evolution of macroscopic quantities of the rock sub-sample of during the dissolution process.

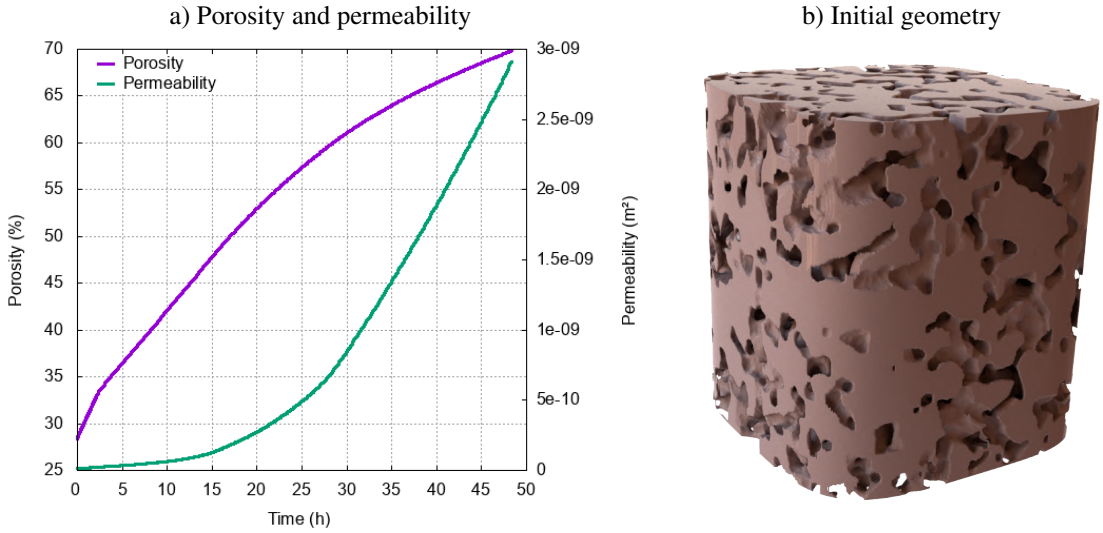

Figure 8: Evolution of macroscopic quantities of the Castlegate rock sub-sample during the dissolution process (left picture), from the initial geometry displayed on right picture.

5.3. Dissolution of a percolating 3D carbonate rock

The third case focuses on the dissolution of a Castlegate sandstone sample [49] at a resolution of 256^3 voxels, displayed on the right picture of figure 7. This dataset is used only as an input geometry and we assume the same 5% porosity for the solid matrix as in section 5.2, so that here the initial porosity is larger than the estimation from [49]. The voxel size is $5.6^3 \mu\text{m}^3$, giving a sample of 1.43mm wide. In this case, the black and white image is simply converted to bang-bang values for ε. An inlet velocity of $u_\infty = 2\,10^{-5}\text{m} \cdot \text{s}^{-1}$ was enforced, corresponding to a mass flow rate of $0.164\mu\text{L} \cdot \text{s}^{-1}$. The specific reactive area is estimated from the pore-solid interface so that $A_s = 8288\text{m}^{-1}$ and the molecular diffusion is set at $D_M = 10^{-10}\text{m}^2 \cdot \text{s}^{-1}$, together with a dissolution constant $K_s = 10^{-2}$.

The absolute permeability of the sample is unknown but an estimated initial permeability of $\widetilde{K} = 1.22\,10^{-11}\text{m}^2$ was obtained with a driving force of $f = 603\text{Nm}^{-3}$, and the initial porosity is computed at $\widetilde{\phi} = 0.284$. This case is characterized by $Pe = 0.7$ and $Da_{II} = 1.2\,10^4$ (that is to say $Da_I = 1.7\,10^4$).

The evolution of permeability and porosity are shown on figure 7. We can observe more regularity than for the non-percolating geometry studied in the previous section, since there is no break-through process. 50 hours of dissolution are simulated, making the porosity grow from 28% to 70%, associated to an increase of permeability. Furthermore, one can observe a dramatic growth of permeability once the porosity reaches 50% (around 20h).

At such a high Dahmköhler number, the dissolution regime is expected to be driven by the Peclet number. According to [51] (their figure 15 on page 476), we expect conical wormholes in the present simulation, the typical feature of $0.01 < Pe < 1$ and $Da_I > 1$, with a Péclet number close to the dominant wormhole regime. To the opposite of the synthetic configurations considered in [51], the present real geometry exhibits a natural ramified structure, consequently leading to an apparently ramified wormholing, as shown on figure 10 up to 12h. Nevertheless, long time

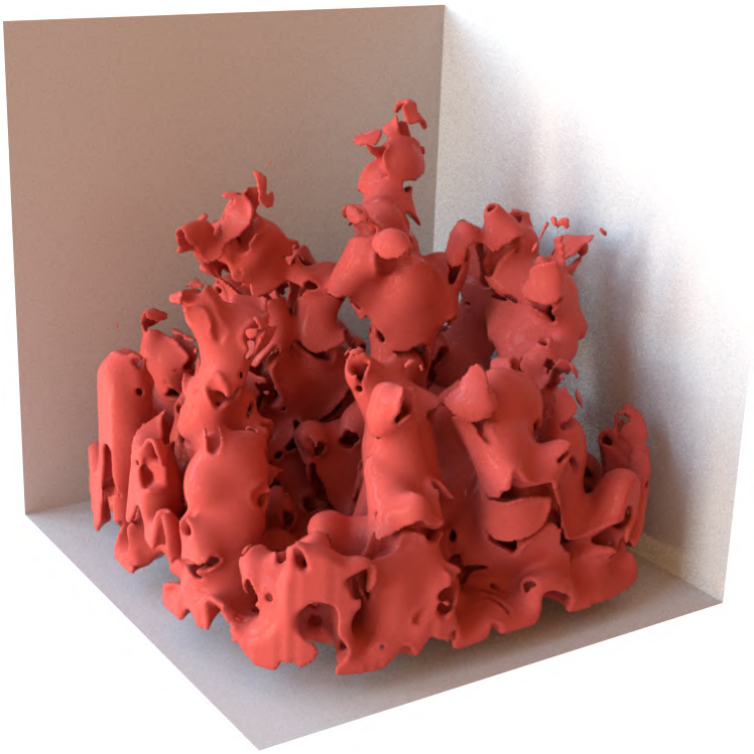

Figure 9: Isolevel of $\partial\varepsilon/\partial t$ at half of its maximum value (1.5810^{-5}), after 12.3h of dissolution, illustrating dominant wormhole regime coupled to the natural ramification of the medium.

scales (more than 40h in our simulation) lead to a set of a few conical wormholes. The evolution of the rock matrix is specifically displayed on the bottom pictures of figure 10. In order to identify more clearly the regime occurring, the time derivation of the local porosity $\partial\varepsilon/\partial t$ is displayed on the figure 9 at time $t = 12.3$h, showing that the dissolution is occurring at the fluid-solid interface and not dispatch over all the pores, featuring a collection of individual conical wormholes. Finally, if the Péclet number was based on a typical size of pore throats, counting roughly 5 pores in the sample width, its resulting value would be 82 time larger, and the coherence with the Péclet number based on the permeability may deserve to be investigated.

6. Conclusions and perspectives

This study focused on the accurate simulation of dissolution processes at pore-scale. This paper presents a transport-diffusion-dissolution model that consistently couples a Lagrangian formulation for the reaction equations with the superficial velocity formalism introduced by Quintard and Whitaker. The present study shows that *a posteriori* kernel selection makes if possible to reconcile accurate interpolation and sign-preservation.

The main outcome is that the method benefits from the quality of particle tracking for the transport, the quality of the particle distribution through the remeshing procedure, and the accurate computation of the diffusion owing to its adaptation to the choice of remeshing kernel. This adaptative diffusion was performed in two steps. First, by selecting a remeshing kernel as a function of the local porosity in order to maximize the interpolation order in fast regions and minimize the spurious diffusion in the rock matrix (physically small due to Archie's law). Second, by adjusting the diffusion coefficient using an *a posteriori* estimation of the spurious diffusion induced by the remeshing procedure.

The robust method developed in this article could be extended naturally to the computation of reactions between fluids with an heterogeneous rheology or plasticity, and to precipitation and crystallization processes. Future studies will focus on the different dissolution regimes in rocks exhibiting ramified pore structures in order to build a coherence with classifications based on synthetic configurations.

Acknowledgments

This work was partially supported by the Carnot Institute ISIFoR with grants by MicroMineral (Contract P450902ISI). For this work, the team was granted access to Pyrene's HPC resources (UPPA Cluster). The authors are ranked by alphabetical order.

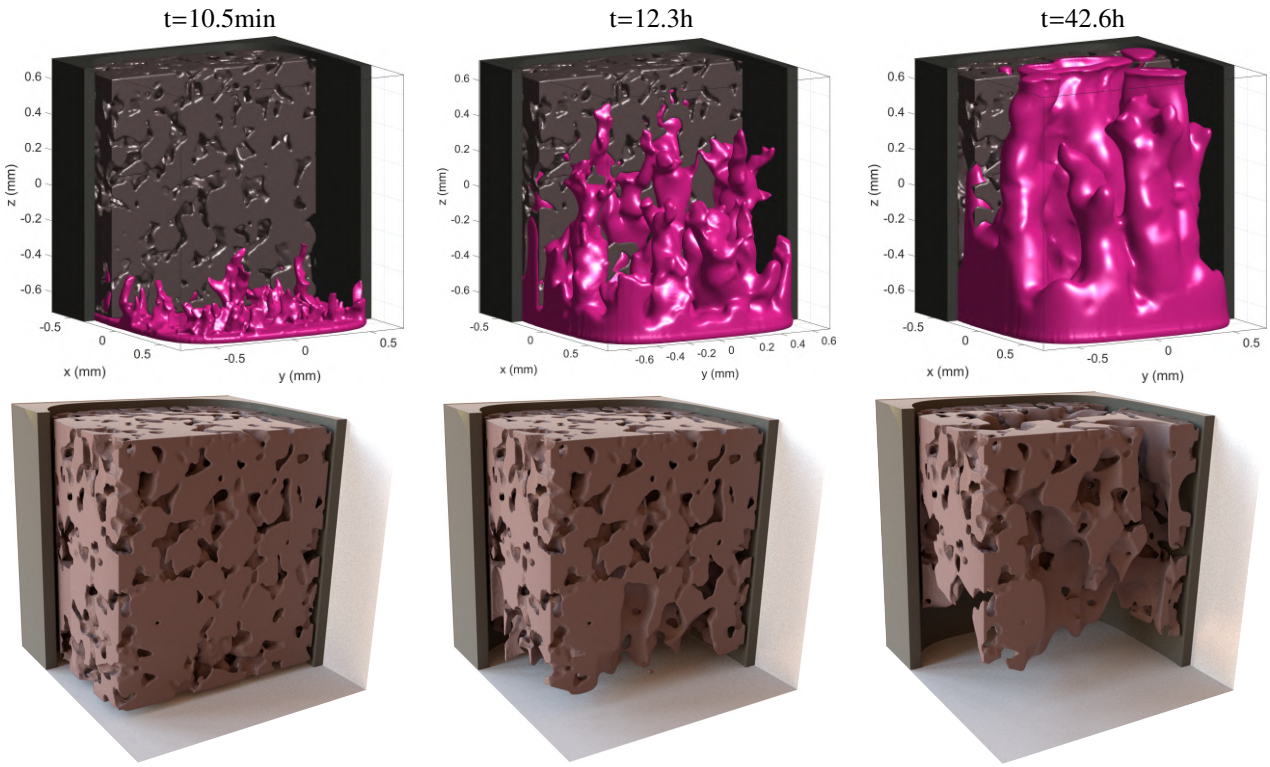

Figure 10: Dissolution process at several times. The top pictures present the evolution of acid level at concentration 10^{-3}mol/L (in magenta), together with the pore-solid interface (colored by its residual acid concentration) and the surrounding carter (in dark gray). Bottom pictures show the erosion of the rock matrix at the same times, cut at 3/4 of its width in order to exhibit internal pore topopoly. The planes delimit the computational box.

References

[1] J.C. Adams. MUDPACK-2: Multigrid software for approximating elliptic partial differential equations on uniform grids with any resolution. *Applied Mathematics and Computation*, 53(2):235 – 249, 1993.

[2] L.T. Akanji and S.K. Matthai. Finite element-based characterization of pore-scale geometry and its impact on fluid flow. *Transp. Porous Med.*, 81:241–259, 2010.

[3] P. Angot, G. Carbou, and V. Péron. Asymptotic study for Stokes-Brinkman model with jump embedded transmission conditions. *Asymptotic Analysis* 96(3-4): 223-249, 2016.

[4] G. E. Archie. The electrical resistivity log as an aid in determining some reservoir characteristics. *Petroleum Transactions of AIME*, 146:54–62, 1942.

[5] C. H. Arns, H. Jiang, H. Dai, I. Shikhov, N. Sayedakram, and J-Y. Arns. A digital rock physics approach to effective and total porosity for complex carbonates: pore-typing and applications to electrical conductivity. *E3S Web Conf.*, 89:05002, 2019.

[6] M.T. Balhoff, S.G. Thomas, and M.F. Wheeler. Mortar coupling and upscaling of pore-scale models. *Comput. Geosci.*, 12:15–27, 2008.

[7] UC Bandara, AM Tartakovsky, M Oostrom, BJ Palmer, J Grate, and C Zhang. Smoothed particle hydrodynamics pore-scale simulations of unstable immiscible flow in porous media. *Adv. Water Res.*, 62:356–369, 2013.

[8] P. Barreau, D. Lasseux, H. Berlin, and A. Zaitowf. Effect of adsorbed polymers on relative permeability and capillary pressure: a pore scale numerical study. *WIT Transactions on Modelling and Simulation*, 10, 1970.

[9] F. Bayram and I. Bektasoglu. Determination of actual dissolution rates from some rock properties in construction of deep salt cavern for natural gas storage. *International Journal of Rock Mechanics and Mining Sciences*, 126:104183, 2020.

[10] P. C. Carman. Fluid flow through granular beds. *Transactions, Institution of Chemical Engineers, London*, 15:150–166, 1937.

[11] A.K. Chaniotis and D. Poulikakos. High order interpolation and differentiation using b-splines. *Journal of Computational Physics*, 197(1):253 – 274, 2004.

[12] R. Chatelin and P. Poncet. A hybrid grid-particle method for moving bodies in 3D stokes flow with variable viscosity. *SIAM Journal on Scientific Computing*, 35(4):B925–B949, August 2013.

[13] G-H. Cottet, J-M. Etancelin, F. Pérignon, and C. Picard. High order Semi-Lagrangian particle methods for transport equations: Numerical analysis and implementation issues. *ESAIM: Mathematical Modelling and Numerical Analysis*, 48(4):1029–1060, 2014.

[14] G-H. Cottet, R. Hildebrand, P. D. Koumoutsakos, C. Mimeau, I. Mortazavi, and P. Poncet. Passive and active flow control using vortex methods. *Proceedings of the 6th International Conference on Vortex Flows and Vortex Models*, Nagoya, Japan, 2014.

[15] G.-H. Cottet and P. D. Koumoutsakos. *Vortex Methods: Theory and Practice*. Cambridge University Press, March 2000.

[16] M. El Ossmani and P. Poncet. Efficiency of multiscale hybrid grid-particle vortex methods. *Multiscale Modeling & Simulation*, 8(5):1671–1690, January 2010.

[17] J-M. Etancelin. *Couplage de modèles, algorithmes multi-échelles et calcul hybride*. PhD thesis, Université de Grenoble, 2014.

[18] S. F. Farshidi, Y. Fan, L. J. Durlofsky, and H. A. Tchelepi. Chemical reaction modeling in a compositional reservoir-simulation framework. *Society of Petroleum Engineers*, 163677, 2013.

[19] L. P. Ferreira, R. Surmas, M. A. P. Silva, and R. P. Peçanha. Carbonates: Porosity and permeability voxel to voxel, doi:10.17612/v09y-aw80. *digitalrocksportal.org*, 2020.

[20] L. P. Ferreira, R. Surmas, S. N. Tonietto, M. A. P. da Silva, and R. P. Peçanha. Modeling reactive flow on carbonates with realistic porosity and permeability fields. *Advances in Water Resources*, 139:103564, 2020.

[21] F. Gray, B. Anabaraonye, S. Shah, E. Boek, and J. Crawshaw. Chemical mechanisms of dissolution of calcite by hcl in porous media: Simulations and experiment. *Advances in Water Resources*, 121:369 – 387, 2018.

[22] Y. Hao, M. M. Smith, and S. A. Carroll. Multiscale modeling of co2-induced carbonate dissolution: From core to meter scale. *International Journal of Greenhouse Gas Control*, 88:272 – 289, 2019.

[23] M. M. Hejlesen, P. Koumoutsakos, A. Leonard, and J. H. Walther. Iterative Brinkman penalization for remeshed vortex methods. *Journal of Computational Physics*, 280:547–562, 2015.

[24] L. Hume and P. Poncet. A velocity-vorticity method for highly viscous 3D flows with application to digital rock physics. *to appear in Journal of Computational Physics*, 2020.

[25] J. Kang, N.I. Prasianakis, and J. Mantzaras. Thermal multicomponent lattice boltzmann model for catalytic reactive flows. *Physical Review E - Statistical, Nonlinear, and Soft Matter Physics*, 89(6), 2014.

[26] J-B. Keck. *Numerical modelling and High Performance Computing for sediment flows*. PhD thesis, Université de Grenoble Alpes, 2019.

[27] S. Khirevich and T. W. Patzek. Behavior of numerical error in pore-scale lattice boltzmann simulations with simple bounce-back rule: Analysis and highly accurate extrapolation. *Physics of Fluids*, 30(9):093604, 2018.

[28] P. Koumoutsakos. Multiscale flow simulations using particles. *Annual Review of Fluid Mechanics*, 37(1):457–487, 2005.

[29] J. Kozeny. Ueber kapillare leitung des wassers im boden. *Sitzungsber Akad. Wiss., Wien*, 136(2a):271–306, 1927.

[30] K. J. Laidler and C. M. King. Development of transition-state theory. *The Journal of Physical Chemistry*, 87(15):2657–2664, 1983.

[31] O. Lehmann, L. Birnhack, and O. Lahav. Design aspects of calcite-dissolution reactors applied for post treatment of desalinated water. *Desalination*, 314:1 – 9, 2013.

[32] L. Li, C. A. Peters and M. A. Celia. Upscaling geochemical reaction rates using pore-scale network modeling. *Advances in Water Resources* 29(3):1351-1370, 2006.

[33] S. Liska and T. Colonius. A fast lattice green's function method for solving viscous incompressible flows on unbounded domains. *Journal of Computational Physics*, 316:360 – 384, 2016.

[34] P. Liu, T. Zhang and S. Sun. A tutorial review of reactive transport modeling and risk assessment for geologic CO2 sequestration. *Computers & Geosciences* 127:1–11, 2019.

[35] Y. Lucas, V. V. Ngo, A. Clément, B. Fritz, and G. Schäfer. Modelling acid stimulation in the enhanced geothermal system of soultz-sous-forêts (alsace, france). *Geothermics*, 85:101772, 2020.

[36] A. Magni and G.-H. Cottet. Accurate, non-oscillatory, remeshing schemes for particle methods. *Journal of Computational Physics*, 231(1):152–172, January 2012.

[37] C. Mimeau, I. Mortazavi, and G-H. Cottet. Passive control of the flow around a hemisphere using porous media. *European Journal of Mechanics - B/Fluids*, 65:213–226, 2017.

[38] S. Molins, C. Soulaine, N. I. Prasianakis, A. Abbasi, P. Poncet, A. J. C. Ladd, V. Starchenko, S. Roman, D. Trebotich, H. A. Tchelepi, and C. I. Steefel. Simulation of mineral dissolution at the pore scale with evolving fluid-solid interfaces: Review of approaches and benchmark problem set. *Computational Geosciences*, 2020, https://doi.org/10.1007/s10596-019-09903-x.

[39] Sergi Molins, David Trebotich, Carl I. Steefel, and Chaopeng Shen. An investigation of the effect of pore scale flow on average geochemical reaction rates using direct numerical simulation. *Water Resour. Res.*, 48(3), mar 2012.

[40] J.J Monaghan. Extrapolating b splines for interpolation. *Journal of Computational Physics*, 60(2):253–262, September 1985.

[41] J. D. Naviaux, A. V. Subhas, N. E. Rollins, S. Dong, W. M. Berelson, and J. F. Adkins. Temperature dependence of calcite dissolution kinetics in seawater. *Geochimica et Cosmochimica Acta*, 246:363 – 384, 2019.

[42] M. K. Panga, M. Ziauddin, and V. Balakotaiah. Two-scale continuum modelfor simulation of wormholes in carbonate acidization. *AIChE Journal*, 51:3231–3248, 2005.

[43] J. P. Pereira-Nunes, M. J. Blunt, and B. Bijeljic. Pore-scale simulation of carbonate dissolution in micro-CT images. *J. Geophys. Res. Solid Earth*, 121(2):558–576, feb 2016.

[44] P. Poncet. Finite difference stencils based on particle strength exchange schemes for improvement of vortex methods. *Journal of Turbulence*, 7:N23, 2006.

[45] P. Poncet. Analysis of direct three-dimensional parabolic panel methods. *SIAM Journal on Numerical Analysis*, 45(6):2259–2297, 2007.

[46] M. Quintard and S. Whitaker. Ecoulement monophasique en milieu poreux : Effet des hétérogénéités locales. *Journal de Mécanique théorique et appliquée*, 6:691–726, 1987.

[47] M. Quintard and S. Whitaker. Two phase flow in heterogeneous porous media: the method of large-scale averaging. *Transport in Porous Media*, 3:357–413, 1987.

[48] D. Sanchez, L. Hume, R. Chatelin, and P. Poncet. Analysis of the 3D non-linear Stokes problem coupled to transport-diffusion for shear-thinning heterogeneous microscale flows, applications to digital rock physics and mucociliary clearance. *ESAIM: Mathematical Modelling and Numerical Analysis*, 53:1083–1124, 2019.

[49] Adrian Sheppard and Masa Prodanovic. Network generation comparison forum. `http://www.digitalrocksportal.org/projects/16`, 2015.

[50] K. Singh, B. U. Anabaraonye, M. J. Blunt, and J. Crawshaw. Partial dissolution of carbonate rock grains during reactive co2-saturated brine injection under reservoir conditions. *Advances in Water Resources*, 122:27 – 36, 2018.

[51] C. Soulaine, S. Roman, A. Kovscek, and H. Tchelepi. Mineral dissolution and wormholing from a pore-scale perspective. *Journal of Fluid Mechanics*, 827:457 – 483, September 2017.

[52] Vitaliy Starchenko, Cameron J Marra, and Anthony J. C. Ladd. Three-dimensional simulations of fracture dissolution. *J. Geophys. Res. Solid Earth*, 121:6421–6444, 2016.

[53] C. I. Steefel, C. A. J. Appelo, B. Arora, D. Jacques, T. Kalbacher, O. Kolditz, V. Lagneau, P. C. Lichtner, K. U. Mayer, J. C. L. Meeussen, S. Molins, D. Moulton, H. Shao, J. Šimůnek, N. Spycher, S. B. Yabusaki, and G. T. Yeh. Reactive transport codes for subsurface environmental simulation. *Computational Geosciences*, 19(3):445–478, Jun 2015.

[54] C. I. Steefel, D. J. De Paolo and P. C. Lichtner. Reactive transport modeling: An essential tool and a new research approach for the Earth sciences. *Earth and Planetary Science Letters*, 240(3):539–558, 2005.

[55] C. I. Steefel and A. C. Lasaga. A coupled model for transport of multiple chemical species and kinetic precipitation/dissolution reactions with application to reactive flow in single phase hydrothermal systems. *American Journal of Science*, 294(5):529–592, 1994.

[56] N. Wakao and J.M. Smith. Diffusion in catalyst pellets. *Chemical Engineering Science*, 17(11):825 – 834, 1962.

[57] L. Wissmeier and D. A. Barry. Effect of mineral reactions on the hydraulic properties of unsaturated soils: Model development and application. *Advances in Water Resources*, 32(8):1241 – 1254, 2009.

[58] H. Yoon, A. J. Valocchi, C. J. Werth, and T. Dewers. Pore-scale simulation of mixing-induced calcium carbonate precipitation and dissolution in a microfluidic pore network. *Water Resour. Res.*, 48(2), feb 2012. W02524.